University of Reading

Soil moisture and soil depth retrieval using the coupled phase-amplitude behaviour of C-band radar backscatter in the presence of sub-surface scattering

Article

Accepted Version

Morrison, K. ORCID: https://orcid.org/0000-0002-8075-0316 and Wagner, W. (2022) Soil moisture and soil depth retrieval using the coupled phase-amplitude behaviour of C-band radar backscatter in the presence of sub-surface scattering. Canadian Journal of Remote Sensing, 48 (6). pp. 779-792. ISSN 1712-7971 doi: 10.1080/07038992.2022.2120858 Available at https://centaur.reading.ac.uk/108023/

It is advisable to refer to the publisher's version if you intend to cite from the work. See Guidance on citing.

To link to this article DOI: http://dx.doi.org/10.1080/07038992.2022.2120858

Publisher: CSP Publishing Services

All outputs in CentAUR are protected by Intellectual Property Rights law, including copyright law. Copyright and IPR is retained by the creators or other copyright holders. Terms and conditions for use of this material are defined in the End User Agreement.

University of Reading

www.reading.ac.uk/centaur

CentAUR

Central Archive at the University of Reading

Reading's research outputs online

Soil Moisture and Soil Depth Retrieval Using the Coupled Phase-Amplitude Behaviour of C-Band Radar Backscatter in the Presence of Sub-Surface Scattering

Keith Morrison[a*] and Wolfgang Wagner[b]

[a*]*Department of Meteorology, University of Reading, P.O. Box 243, Reading RG6 6BB, UK.* (e-mail: k.morrison@reading.ac.uk) **corresponding author*.

[b]*Department of Geodesy and Geoinformation, TU Wien, Wiedner Hauptstraße 8-10, Vienna 1040, Austria* (e-mail: Wolfgang.Wagner@geo.tuwien.ac.at).

Soil Moisture and Soil Depth Retrieval Using the Coupled Phase-Amplitude Behaviour of C-Band Radar Backscatter in the Presence of Sub-Surface Scattering

Abstract: In low-moisture regimes, strongly-reflecting bedrock underlying a soil could provide a dominant return. This offers a novel opportunity to retrieve both the volumetric moisture fraction (m_v) and depth (d) of a soil layer using differential phase. A radar wave traversing the overlying soil slows in response to moisture state; moisture dynamics are thus recorded as variations in travel time - captured back at a radar platform as changes in phase. The Phase Scaled Dielectric (PSD) model introduced here converts phase changes to those in soil dielectric as an intermediate step to estimating m_v. Simulations utilising a real soil moisture timeseries from a site in Sudan were used to demonstrate the linked behaviours of the soil and radar variables, and detail the PSD principle. A laboratory validation used a soil with a wet top layer variable in depth 1-2 cm and drying from m_v~0.2 m^3m^{-3}, overlying a gravel layer at a depth of 11 cm. The scheme retrieved d=1.49 ± 0.33 cm and a change Δm_v = 0.191-0.021 ± 0.009 m^3m^{-3}. The PSD scheme outlined here promises a new avenue for the diagnostic measurement of soil parameters which is not currently available to radar remote sensing.

Keywords: SAR, phase scaled dielectric, soil moisture, sub-surface, GPR

1. Introduction

The regular and synoptic retrieval of soil moisture has entered in-service operation. At the forefront are products such as those provided by the European Organisation for the Exploitation of Meteorological Satellites (EUMETSAT), and the European Space Agency (ESA). EUMETSAT's Satellite Application Facility on Support to Operational Hydrology and Water Management facility (H SAF) provides daily products delivered in near-real time, based solely on incoherent C-band backscatter from the Advanced Scatterometer (ASCAT) satellite (Massari et al. 2015; Wagner et al. 2013). In contrast, ESA's Climate Change Initiative Soil Moisture product ingests data from a variety of passive and active sensors to provide daily soil moistures, although delivered weeks or months post-measurement (Dorigo et al. 2017; Gruber et al. 2019). Whilst the radar-based products show encouraging agreements with spatial and temporal behaviours estimated by land surface models and in-situ observations, persistent problems remain with some

anomalous regions (Naeimi et al. 2009; Dostálová et al. 2014; Lindell and Long 2016; Hahn, Melzer, and Wagner 2012; Rodell et al. 2004). Particularly problematic are regions of the world associated with hot arid zones and low soil moisture regimes. Previous work has explained these anomalies can arise from the presence of significant sub-surface scattering. This is dominant at times of low moisture conditions (Morrison 2013; Liu et al. 2016; Morrison and Wagner 2020) when reduced attenuation from the overlying soil allows enhanced scattering from the sub-surface features. This can lead to distortion - or even inversion - of expected soil moisture backscatter curves, such that these areas currently do not provide operational radar-derived products. These regions represent some of the most fragile environments of the planet. Many are suffering climate-related temperature increases significantly above the global averages and face increasingly variable rainfall leading to more frequent droughts (Thomas and Nig 2017; Wang and Yan 2017).

In the last decade, researchers have begun to look more closely at interferometric phase to extract soil properties. There has been a marked increase in the availability of satellite interferometric synthetic aperture radar (SAR) products, particularly from Sentinel-1 which typically provides a 6- or 12-day repeat pass capability (Torres et al. 2012; Prats-Iraola et al. 2017; Ullman et al. 2019; Kellndorfer et al. 2022; ESA Earth Online 2022a; ESA Earth Online 2022b). The research activity splits naturally into two groups: The first treats phase as a summation of scattering from the volume of a soil layer in order to extract soil moisture (De Zan et al. 2014; Zwieback et al. 2017; Zwieback, Hensley, and Hajnsek 2017). The second group does not directly measure soil moisture per se, but rather use it to identify buried features or enhance sub-surface imaging (Lasne et al. 2004; Morrison 2013; Morrison, Bennett, and Nolan 2013; Morrison and Bennett 2015). Additionally, the latter group's work is concerned with low-moisture conditions appropriate to the arid regions of the world of interest here.

In this paper, we build upon the work of the second group to develop a coherent model of sub-surface scattering in low moisture regimes, able to estimate both soil moisture and the thickness of the active soil layer.

2. The Model

2.1 Radar Wave Propagation: The workings of the model are structured around the behaviour of the complex propagation constant, γ, of a radar wave passing through a soil.

Consider the propagation of a complex radar signal, $\boldsymbol{S}$, shown in Figure 1 which has incidence onto a soil at an angle *i*, and is transmitted into it at an angle *t*. It reflects from a point P on the underlying bedrock. Its two-way propagation through the soil is described by;

$$\boldsymbol{S}(z) = \boldsymbol{S_0}\, exp(-2\frac{\gamma z}{cos\, t}) \tag{1}$$

where $\boldsymbol{S_0}$ is the unattenuated signal at the soil surface, *z* is the vertical distance from the surface, and $\gamma=\alpha + j\beta$ is the complex propagation constant. The α term relates to the attenuation of the signal, and the β term to the phase of the propagating signal. The soil is modelled as a lossy homogeneous dielectric medium with a relative complex dielectric constant $\varepsilon = \varepsilon_r + j\varepsilon_i$, where the subscripts *r* and *i* represent the real and imaginary components, respectively. From Morrison and Bennett (2015), the propagation terms can be described solely by the soil's dielectric properties scaled by the wave number, *k*;

$$\alpha = k\sqrt{\varepsilon_r}[(1 + tan^2\,\delta)]^{\frac{1}{4}} sin\left(\frac{\delta}{2}\right) \tag{2}$$

$$\beta = k\sqrt{\varepsilon_r}[(1 + tan^2\,\delta)]^{\frac{1}{4}} cos\left(\frac{\delta}{2}\right) \tag{3}$$

where $k = 2\pi/\lambda$, λ is the free-space wavelength, and δ is related to the loss tangent term via $tan\,\delta = \varepsilon_i/\varepsilon_r$. The absolute, unwrapped phase Φ associated with passage through the soil is related to the β term;

$$\begin{aligned}\Phi &= 2\beta\frac{z}{cos\, t}\\ &= 2k\sqrt{\varepsilon_r}\, cos\left(\frac{\delta}{2}\right)\frac{z}{cos\, t}\end{aligned} \tag{4}$$

We have dropped the $[(1 + tan^2\,\delta)]^{\frac{1}{4}}$ term to provide a more compact equation, as it is very close to 1 for the moisture regimes of interest here (Morrison and Bennett 2015). Similarly, the backscatter amplitude $|\boldsymbol{S}|$ is related to the α term;

$$\begin{aligned}|\boldsymbol{S}| &= |\boldsymbol{S_0}|\, exp(-2\alpha\frac{z}{cos\, t})\\ &= |\boldsymbol{S_0}|\, exp\left\{-2k\sqrt{\epsilon_r}\, sin\left(\frac{\delta}{2}\right)\frac{z}{cos\, t}\right\}\end{aligned} \tag{5}$$

where $|\boldsymbol{S}|$ is calculated purely considering attenuation of the signal from its two-way passage through the soil.

It is the measurement of phase across a timeseries that forms the basis of the model. Figure 2 shows how the physical depth, *d*, of the soil is sensed by a radar to have increased by the factor $\sqrt{\varepsilon_r}$. Variations in the dielectric term on the timescale of days to months can be expected to be controlled solely by the variations in moisture. From Equation 4, these produce concomitant variations in Φ, measured as a differential phase ΔΦ record as the moisture moves between the moisture minimum and maximum states.

2.2 Phase Scaled Dielectric: Figure 3 shows the modelled $\sqrt{\varepsilon_r}$, Φ, m_v behaviours and dependencies at 6 GHz using Equation 4, for a homogenous sandy soil with a thickness *d*=0.05m, overlying bedrock which behaves as a point scatterer. The model utilises the work of Hallikainen et al. (1985) which details how soil dielectric is controlled by the volumetric water content, m_v. Hallikainen et al. provides tables of polynomial coefficients to estimate ε_r and ε_i – and related δ term - for different soil textures (the percentage fractions of sand, clay, and silt in a soil). The $\sqrt{\varepsilon_r}$–Φ- m_v relationships are close to linear, but with some slight deviation below around m_v=0.05 m^3m^{-3}.

With reference to Equation 4, consider the ratio of Φ at two times and rearrange it to express the relative real dielectric;

$$\sqrt{\varepsilon}_{r,n} = \sqrt{\varepsilon}_{r,min} \frac{cos\left(\frac{\delta_{min}}{2}\right) cos\, t_n}{cos\left(\frac{\delta_n}{2}\right) cos\, t_{min}} \left[\frac{\Phi_n}{\Phi_{min}}\right] \quad (6)$$

where we have set measurement 1 to be at a minimum moisture condition, and the second measurement is the *n*th in a sequence. In a real-world application, the cosine terms would be unknown. It is assumed $\sqrt{\varepsilon}_{r,min}$ is a known constant and relates to its value at m_v=0.02 m^3m^{-3} from Hallikainen et al. 1985. The Φ terms are obtained from the data. For the soil moisture regimes considered in this study, $m_v \leq 0.2$, and the $cos\left(\frac{\delta_{min}}{2}\right) / cos\left(\frac{\delta_2}{2}\right)$ term is always very close to 1. Hence, we can write;

$$\sqrt{\varepsilon}_{r,n} = \sqrt{\varepsilon}_{r,min} \frac{cos\, t_n}{cos\, t_{min}} \left[\frac{\Phi_n}{\Phi_{min}}\right] \quad (7)$$

At nadir we can we omit the remaining cos(.) terms in Equation 7, and write;

$$\sqrt{\varepsilon}_{r,n} = \sqrt{\varepsilon}_{r,min} \left[\frac{\Phi_n}{\Phi_{min}}\right] \qquad (i = 0°) \quad (8)$$

Equation 8 informs us that the dielectric term at any moisture state can be related to the reference dielectric term $\sqrt{\varepsilon}_{r,min}$ at moisture minimum scaled by a phase term. We henceforth refer to this as the *phase scaled dielectric* (PSD) approach. $\sqrt{\varepsilon}_{r,n}$ can be inverted to obtain m_v using the m_v - $\sqrt{\varepsilon}_r$ relationship displayed in Figure 3, and which is described by;

$$m_v = 0.2074\sqrt{\varepsilon_r} - 0.0368\sqrt{\varepsilon_r}^2 + 0.00439\sqrt{\varepsilon_r}^3 - 0.2368 \qquad (9)$$

Away from nadir, omission of the unknown $cos\, t_n / cos\, t_{min}$ term leads to increasing underestimation of $\sqrt{\varepsilon}_{r,n}$, as shown in Figure 4. Utilizing the full expression for $\sqrt{\varepsilon}_{r,n}$ in Equation 6, we can rewrite the cos(δ) and cos *t* terms in their ε_r forms using the relationships in Hallikainen et al. and Snell's Law, respectively, and solve for the value of $\varepsilon_{r,n}$ that satisfies both sides of Equation 6. A satisfactory analytical representation is found for viewing geometries from nadir up to 40°:

$$\sqrt{\varepsilon}_{r,n} = \sqrt{\varepsilon}_{r,min}\left[\frac{1}{\sqrt{cos\, i}}\left(\frac{\Phi_n}{\Phi_{min}} - 1\right) + 1\right] \qquad i \leq 40° \qquad (10)$$

Importantly, the expression for $\sqrt{\varepsilon}_{r,n}$ is now written only in terms of known (*i*) or measured (Φ) values. The difference residuals between Equations 6 and 10 are lower than 1%.

For $i > 40°$, retrieval of $\sqrt{\varepsilon}_{r,n}$ is a two-stage process. Firstly, estimate a faux provisional value of the dielectric term, $\sqrt{\varepsilon}_{r,n}'$, utilizing the equation for *i*=0° in Equation 8, but using the measured Φ values for the angle of interest. Then apply a correction to each provisional value using a third-order polynomial $f(\sqrt{\varepsilon_r}) = a\sqrt{\varepsilon_r} + b\sqrt{\varepsilon_r}^2 + c\sqrt{\varepsilon_r}^3 + d$ defined in Table 1, such that the final true value is given by;

$$\sqrt{\varepsilon}_{r,n} = f\sqrt{\varepsilon}_{r,n}' \qquad i > 40° \qquad (11)$$

3. Timeseries Simulation

3.1 Data set: To further develop and demonstrate the performance of the model, it was applied using an illustrative real-world soil moisture timeseries. The 5cm-depth soil moisture record from a water content reflectometer CS616 (Campbell Scientific) was obtained for Demokeya (13.3°N, 30.5°E), Sudan (Ardo 2013). The data is supplied as

part of the International Soil Moisture Network (https://ismn.geo.tuwien.ac.at/en/) (Dorigo et al. 2021). Figure 5 is a composite map of North and Central Africa and the Middle East, which shows the locations of previously reported permanent (brown) and seasonal (green) soil moisture anomalies (Morrison & Wagner 2020), overlain on the European Space Agency's (ESA) Climate Change Initiative (CCI) global soil texture map. The location of Demokeya is marked, which shows it lies south of the anomalous moisture zone. It has a mean annual precipitation of 320mm, concentrated between June to October. The soil is 97% sand and 3% silt. Figure 6a shows the moisture record for 2006, recorded at 30-minute intervals, and which ranged between 0.021 - 0.140 m^3m^{-3}.

3.2 Model Parameters: The model used a 0.05m thick, 100% sandy soil above a buried reflecting layer which behaved as a deterministic point scatterer. Adopting the Demokeya m_v curve and using an incidence angle, i=25°, we estimate the corresponding Φ, $\sqrt{\varepsilon}_r$, and $|\boldsymbol{S}|$ timeseries at 6 GHz, respectively, as shown in Figure 6b, d, e. They indicate how the modelled parameters clearly follow the m_v curve. Additionally, Figure 6c shows the wrapped differential phase that would be measured in a real-world application. Figure 6f shows the near linear relationship between phase and logarithmic power, using the data from 6b and 6e.

A minimum moisture was identified on day 79. We choose that a minimum always occurs at m_v=0.02 m^3m^{-3} with $\sqrt{\varepsilon}_{r,min}$=1.630. In further support of the choice of m_v=0.02 m^3m^{-3} rather than m_v=0.00 m^3m^{-3}, in laboratory studies we have to adopt m_v=0.02 m^3m^{-3} in order to get best agreement between modelled and measured dielectric (Edwards et al. 2017). In arid regions, minimum moisture conditions persist over extended time intervals and so should be easy to identify. In addition, consideration of Equations 4 and 5 tells us that backscatter would be at a maximum when phase is at a minimum, and vice versa. Unlike the case for conventional topographic phase unwrapping (Goldstein, Zebker, and Werner 1988; Chen and Zebker 2001), we have extra information available from the $\Delta|\boldsymbol{S}|$-$\Delta\Phi$ relationship in Figure 6f. Increasing phase is always associated with decreasing backscatter. With this information, it was a simple matter to robustly unwrap the phase in Figure 6c – specifically at the large jump between adjacent data points on Day 197.

3.3 Moisture Determination: Equations 9 and 10 were used with the data in Figure 6 to estimate m_v. The resulting PSD-derived m_v curve shown in Figure 7 agrees well with the

field data in Figure 6a, giving us confidence in the PSD approach. That the disagreement between the curves grows for increasing moisture is to be expected as the measured and modelled curves are forced into agreement at m_v=0.02 m^3m^{-3}. Arbitrary slight changes in the value of $\sqrt{\varepsilon}_{r,min}$ did improve the fit. However, without further scientific justification, we retain the original $\sqrt{\varepsilon}_{r,min}$=1.630 in further analysis.

The model presented above assumed soils with no clay content. The effect on m_v estimation through erroneous assumption of soil texture, is to retain the shape characteristics of the moisture curves but to increasingly underestimate m_v for increasing clay content. However, Figure 5 shows that the assumption of minimal clay content in anomalous zones is very largely correct. The scheme does not seem applicable, however, to saline soils which have high loss tangents through increased electrical conductivity (Li et al. 2014; Paillou et al. 2014).

4. Laboratory Verification

In this section we apply the PSD scheme to a laboratory study of a drying soil. In the simulations above we had the luxury of full knowledge of soil and radar parameters and so were able to properly retrieve soil parameters without ambiguity. The real-world, however, introduces limitations on the information available to us, hampering retrieval of soil parameters. It requires additional processing steps and analysis.

4.1 Laboratory Study: Morrison and Wagner (2020) reported the results of a laboratory polarimetric C-band study of the differential backscatter behaviour, $\Delta|\boldsymbol{S}|$, of arid soils using the indoor microwave measurement facility at the University of Reading. It comprises a 4m roof-mounted, linear microwave scanner that runs downs the centre line of a 4m (l) x 1m (w) x 0.5m (h) soil trough. A 3m x 1m area of gravel was buried under 11cm of dry, 100% sandy soil, the surface of which was smoothed off level with the top of the trough. To collect microwave imagery, the antenna was stepped at 2cm intervals along the scanner. At each of the 235 stepped positions, an HP8720 ES Vector Network Analyser radar unit was swept across a 5.75-6.25 GHz bandwidth. The 0.5 GHz bandwidth only provided a free-space range resolution of 0.3m, such that the surface and sub-surface features were unresolved in the imagery. Thus, both backscatter amplitude and phase were always a summation of the surface and sub-surface signals.

At the start of the experiment, a 4mm depth of water was added across the surface of the first 3m length of the trough. Morrison and Wagner (2020) noted the water only travelled down 1-2cm, producing a sharp boundary between the thin overlying wet layer and the lower, thicker 9cm dry layer, as detailed in Figure 8. Within the wet layer, m_v would have been around 0.2 m^3m^{-3}. Over the next 15 days as the soil dried, the tomographic profiling (TP) scheme (Morrison and Bennett 2013; Edwards-Smith et al. 2017) was used to capture 167 images. TP is a SAR-like imaging technique designed specifically for gathering vertical backscattering profile data through biogeophysical volumes. Unlike in SAR imaging, the antennas are aligned along-track and so only collect data for a transect directly below the scanner. Post-measurement, the antenna beam is synthetically sharpened by coherent summation across a sub-aperture of sample points. This captures a series of vertical 'sounding profiles' through the soil to produce an image transect along the trough length. The sharpened beam can be steered in angle within the physical extent of the real beam by applying phase ramps across the sub-aperture samples, here providing reconstructions 0°-25°. Figure 9 illustrates the experimental data collection.

Figure 10 summarizes the TP results for i=0°, 5°, 10°, 15, 20°, and 25° over the entire drying period. Each of the 167 columns captures the mean backscatter with height from a single scan - such that the illustrative TP scan in Figure 9 would contribute one column, having been averaged horizontally along the transect over the soil region of interest at each height. Adding the results from successive scans provides a montage which allows us to see any changes in the vertical backscatter patterning with time. Below 10°, the results show that the dominant return was always from the surface, and which became weaker as the soil dried. The 10° case showed a transitional behaviour, whereby initial surface dominance gave way to a dominant sub-surface return. Above 10°, the sub-surface return was dominant. The behaviours are as expected; a strong surface return is expected close to nadir, here enhanced by the flat surface of the soil. Away from nadir, the surface return is increasingly forward scattered and lost. As the soil dries, the increasing penetration into the soil enhances the sub-surface signal from the rough-surfaced gravel.

4.2 Differential Phase: The extracted differential phase histories in Figure 11 all show the presence of a deterministic phase across the timeseries. The phase behaviours are in agreement with those expected from the $\Delta|\boldsymbol{S}|$ vertical patterning of Figure 10. The 0° and

5° cases are dominated by a surface return which shows little phase variation. The 10° case shows a return which begins to switch to a sub-surface return after sample 80, characterised by a continuously decreasing phase thereafter. The 15° and above angles had dominant sub-surface returns, and hence characteristic sub-surface phase behaviours from the outset. The spikes in the phase at the start of the experiment correspond to the addition of water.

4.3 Estimating Φ_{min}, d : To be able to use the PSD scheme of Equation 10, we need to recover the unwrapped Φ phase terms, such that they are a measure of the electrical path through the soil. However, the measurements only provide the differential timeseries, ΔΦ, and a direct measurement of Φ_{min} is not possible. To estimate Φ_{min} we look towards the coupled amplitude-phase behaviour highlighted in Figure 6f. Equations 4 and 5 describe the phase and signal amplitude behaviours, respectively, of a radar wave propagating through a soil. If we rewrite Equation 5 as the natural logarithm of the signal $|\boldsymbol{S}|$, and divide it by the phase given by Equation 4, it gives us the convenient relationship;

$$\frac{log_e|\boldsymbol{S}|}{\Phi} = \frac{-sin(\delta/2)}{cos(\delta/2)} \tag{12}$$

Here, $|\boldsymbol{S}|$ has been normalised by setting $|\boldsymbol{S_0}|$=1 in Equation 5, and so is also a direct representation of attenuation. Rearranging, we can see that phase can be considered a manifestation of attenuation, and vice versa:

$$\Phi = -\frac{log_e|\boldsymbol{S}|}{tan\left(\frac{\delta}{2}\right)} \tag{13}$$

Figure 12 plots ΔΦ against $\Delta|\boldsymbol{S}|$ in decibels for the laboratory data at *i*=15°, indicating a strong correlation between the two.

The issue with using Equation 13 in a real-world scenario is that we do not know the absolute attenuation from the measured backscatter (as required by adopting $|\boldsymbol{S_0}|$=1 above), only the differential change, $\Delta|\boldsymbol{S}|$. We assume it is related to the true signal by a multiplicative factor, *m*, $|\boldsymbol{S}| = m\Delta|\boldsymbol{S}|$, Re-writing Equation 13 in terms of the signal amplitude for an arbitrary *nth* state gives:

$$|\boldsymbol{S_n}| = m\Delta|\boldsymbol{S_n}| = exp\left\{-tan\left(\frac{\delta_n}{2}\right)\Phi_n\right\} \tag{14}$$

Dividing this by the signal at minimum moisture state provides;

$$\frac{\Delta|\mathbf{S_n}|}{\Delta|\mathbf{S_{min}}|} = exp\left\{tan(\frac{\delta_{min}}{2})\,\Phi_{\min} - tan(\frac{\delta_n}{2})\,\Phi_{\mathrm{n}}\right\} \quad (15)$$

where division conveniently removes the unknown *m* term. Knowing that the absolute unwrapped phase is the summation of that at moisture minimum and the observed, unwrapped differential change from the minimum, $\Phi_{\mathrm{n}} = \Phi_{\min} + \Delta\Phi_{\mathrm{n}}$ (and $\Delta\Phi_{\min}$ is set to be 0), then;

$$\frac{\Delta|\mathbf{S_n}|}{\Delta|\mathbf{S_{min}}|} = exp\left\{tan(\frac{\delta_{min}}{2})\,\Phi_{\min} - tan(\frac{\delta_n}{2})(\Phi_{\min} + \Delta\Phi_{\mathrm{n}})\right\} \quad (16)$$

The left-hand side (LHS) of Equation 16 is provided directly from the measurements as the ratio of the backscatter amplitudes. On the RHS, δ_{min}=0.0490 is set from the earlier choice of $\sqrt{\varepsilon}_{r,min}$= 1.630 at m_v=0.02 m^3m^{-3} using the relationships given in Hallikainen et al. (1985). In order to solve for $\Phi_{\min}$ we use the identity $|LHS - RHS| = 0$ for Equation 16, iterating through choices of $\Phi_{\min}$ to find that which satisfies the identity. (the choice of $\Phi_{\min}$ sets δ_n through $\sqrt{\varepsilon}_{r,n}$ in Equation 10, from Hallikainen et al.)

Only the first 1-140 samples are used of the 167 available data samples, as Figure 11 shows the phase becomes flat after around sample 140 (associated with reaching a constant minimum moisture state). In addition, for the 10° case, because the first part of the phase history is associated with a surface return in Figure 10, only samples 80-140 are used. Figure 13 shows the retrieved solutions for $\Phi_{\min}$, converted to a wet soil layer depth, *d*, by re-arranging Equation 4 at moisture minimum:

$$z = d = \frac{cos\ t_{1min}\,\Phi_{\min}}{2k\sqrt{\varepsilon}_{r,min}\,cos\left(\frac{\delta_{min}}{2}\right)} \quad (17)$$

$$= \frac{cos\ t_{1min}}{409.54}\,\Phi_{\min} \quad (18)$$

Using moisture minimum allows us to calculate the denominator using the known values $\sqrt{\varepsilon}_{\mathrm{r,min}}$ and $\delta_{\min}$, and with *k*=125.66 (at 6 GHz). The t_{1min}term is viewing-geometry dependent and is calculated using Snell's Law:

$$t_{1min} = sin^{-1}\left(\frac{\sin\ i}{\sqrt{\varepsilon}_{r,min}}\right) = sin^{-1}\left(\frac{\sin\ i}{1.630}\right) \quad (19)$$

The figure shows how the derived solutions for *d* evolve for a changing sample population. The sections of accepted solution are indicated in bold. Regions of rapid change were excluded, such that only values ≤ 0.02m were accepted. Only the 15° case provided a solution for *d* over the entire range. Derived mean *d* values for 10°, 15°, 20°,

25° were 0.0180m, 0.0145m, 0.0104m, 0.0167m, (Φ_{min}= 7.467, 6.015, 4.356, and 7.029 rad), respectively, providing an overall mean of $\bar{d}$=0.0149 ± 0.0033m. The result is in excellent agreement with the observed 1-2cm wet layer depth.

An important comment is that the Equation 16 scheme assumes $|\Delta \boldsymbol{S}|$ is only controlled by attenuation. In practice, $|\boldsymbol{S}|$ in Equation 5 would be better described by $|\boldsymbol{S}'|$ to additionally consider scattering losses at layer interfaces;

$$|\boldsymbol{S}'| = |\boldsymbol{S}| T^2 R_G \tag{20}$$

where T (0-1) is the transmission coefficient at the air-surface interface, and additionally R_G (0-1) describes the reflectivity of the sub-surface layer. Rough surfaces add a complication to use of the Fresnel equations to estimate T, and the reader is referred to De Roo and Ulaby (1996) who recommend a modified physical optics model. Whilst R_G is unknown, we can expect it to be a constant during drying for any given i, as from Snell's Law we can write;

$$sin\ t_2 = \sin i\ / \sqrt{\varepsilon}_{dry} \tag{21}$$

showing that the transmission angle into the dry layer depends only upon the surface incidence angle and the refractive index of the dry layer - it is independent of the wet layer.

4.4 Moisture Retrieval: The solutions for $\Phi_{\min}$ can now be substituted into Equation 10 to calculate $\sqrt{\varepsilon}_{r,n}$, then $\sqrt{\varepsilon}_{r,n}$ converted to m_v using Equation 9. Figure 14a shows the derived m_v timeseries at each incidence angle, using the set of derived d solutions. All curves display a continuously reducing m_v as expected, and which ends up back at the initial dry situation of m_v=0.02 m^3m^{-3}. As expected, the 10° case initially displays a behaviour dominated by a surface return - in agreement with Figure 10 - until around sample 80, after which it begins to follow a sub-surface behaviour in good agreement with the other angles. The 20º case gives notably higher moisture conditions over the first half of the experiment compared to the 15º and 25º cases. If all the added water formed a $\bar{d}$ = 0.0149m layer it would produce m_v=0.269 m^3m^{-3}. The 20º curve peaks very close to this at m_v=0.265 m^3m^{-3}. However, this is very likely an overestimation. Spillage and non-uniform addition between the trough centre and edges will have reduced the moisture

centrally down the centre of the trough sensed by the radar, moving m_v towards 0.20 m^3m^{-3}.

The offsets between curves arise primarily due to differences in the estimation of *d*. The general lack of overlap of the curves in Figure 14a points to systematic biases in the *d* estimates. Figure 14b shows the 15º, 20º, and 25º curves plotted adopting the common average $\bar{d}$=0.0149m. This notably shifts the 20º and 25º curves together, and there is especially good agreement between the three curves over the mid-range values m_v=0.08-0.14 m^3m^{-3}.

5. Discussion

The work presented above points the way for the retrieval of soil moisture based on the coupled behaviour of backscatter phase and amplitude involving sub-surface reflection. The determination of $\Phi_{\min}$ (or equivalently, *d*) is a critical stage, as errors here scale to larger errors at higher m_v. The spread of *d* values in Figure 14 points to the need to better understand the coupled $\Phi - |\boldsymbol{S}|$ behaviour in real-world systems. More advanced optimization techniques with contextual data assimilation should be applied to the problem.

The two-layer experimental set-up here saw the reflecting sub-surface illuminated at a constant incidence angle, due to a constant-moisture lower layer. Simplistically, a one-layer soil would see the illumination (i.e. transmission) angle onto the reflecting sub-layer change (other than at nadir) as the moisture varies. However, whilst the near-surface zone can be expected to suffer large fluctuations in moisture, deeper zones would experience less. The presence of a lower, near-static moisture band could ensure near constant-angle illumination of the reflecting layer, preserving phase coherence.

The two-layer model examined in the laboratory maintained a fixed *d*, but rainfall events would see this fluctuate with time, which must impact on the efficacy of the moisture retrieval. The presence of additional reflectors in the soil volume – such as from air pockets or stones – would alter the interpretation of the signal, where *z* is now likely an average, virtual depth.

There are obviously still many challenges to a real-world exploitation of this work for satellite-based in-service monitoring. The scheme would first require inspection of a historical timeseries (nominally a year) to identify times of minimum moisture to initialise $\Phi_{\min}$. A comparative study should be made of the three primary interferometric schemes to understand their efficacies here, namely Permanent scatterer (PS) (Ferretti, Prati, and

Rocca 2001), small baseline subset (SBAS) (Berardino et al. 2002), and intermittent SBAS (ISBAS, now known as APSIS) (Bateson et al. 2005). Because the PSD scheme is concerned with attenuated signals, it may be limited at times by the challenging noise equivalent sigma zero (NESZ) ~ -25dB of SAR satellites.

Provision of a timeseries which is densely sampled in time is a significant aid in the proper interpretation of any natural variable, important here because soil moisture can change on timescales under a day. Current SAR satellite platforms provide high resolution mapping, but with comparatively low temporal sampling. Imagery availability from Sentinel-1 over almost all the anomalous zones identified in Figure 1, for example, is currently every 12 days. Complimentary concomitant L- and X-band time sequences could help to increase sampling and would also aid in solving $\Phi_{\min}$ ambiguities (Bamler and Eineder 2005). The CCI soil product should be used as an overlay to ensure use of the proper soil texture with location, to derive the proper moisture-phase relationships.

6. Conclusions and Future Work

The work above has outlined a novel scheme for the extraction of soil moisture utilizing the coupled amplitude-phase behaviour of backscatter associated with a dominant sub-surface return, applicable to arid regions. There is much to be gained by further laboratory investigation, paying attention to the possible decorrelating effects of a single wet layer soil. It would also be useful to revisit and scrutinize soil dielectric behaviours reported in Hallikainen et al. (1985), especially with regard to $\varepsilon_{\mathrm{r,min}}$ values for different soil textures. DInSAR satellite timeseries at locations within the soil moisture anomaly zones should be scrutinized to seek out those indicative of coupled $\Delta\Phi - \Delta|\boldsymbol{S}|$ sub-surface behaviours.

7. Acknowledgments

The experimental data used here were originally collected under the European Space Agency's Climate Change Initiative: Soil Moisture, contract 4000112226/14/I-NB.

Data Availability Statement

The data that support the findings of this study are available from the corresponding author, KM, upon reasonable request.

References

Ardö, J. 2013. “A 10-Year Dataset of Basic Meteorology and Soil Properties in Central Sudan.” *Dataset Papers in Geosciences, Article ID 297973*. http://dx.doi.org/10.7167/2013/297973.

Bamler, R. and Eineder, M. 2005. “Accuracy of differential shift estimation by correlation and split-bandwidth interferometry for wideband and delta-k SAR systems.” *IEEE Geoscience and Remote Sensing Letters*, vol. 2, no. 2, pp. 151–155.

Bateson, L., Cigna, F., Boon, D., and Sowter, A. 2005. “The application of the intermittent SBAS (ISBAS) InSAR method to the South Wales Coalfield, UK.” *Int. J. Appl. Earth Obs. Geoinf.* 34, 249–257. https://doi.org/10.1016/j.jag.2014.08.018.

Berardino, P., Fornaro, G., Lanari. R., and Sansosti, E. 2002. "A new algorithm for surface deformation monitoring based on small baseline differential SAR interferograms," *IEEE Trans on Geoscience and Remote Sensing*, vol. 40, no. 11, pp. 2375-2383. doi: 10.1109/TGRS.2002.803792.

Chen, C.W., and Zebker, H.A. 2001. "Two-dimensional phase unwrapping with use of statistical models for cost functions in nonlinear optimization." J. Opt. Soc. Am. A 18, 338-351. https://doi.org/10.1364/JOSAA.18.000338.

De Roo, R. D., and Ulaby, F.T. 1996. "A modified physical optics model of the rough surface reflection coefficient," *IEEE Antennas and Propagation Society International Symposium Digest*, vol. 3, pp. 1772-1775. doi: 10.1109/APS.1996.549946.

De Zan, F., Parizzi, A., Prats-Iraola, P., and López-Dekker, P. 2014. "A SAR Interferometric Model for Soil Moisture." *IEEE Transactions on Geoscience and Remote Sensing*, vol. 52, no. 1, pp. 418-425. doi: 10.1109/TGRS.2013.2241069.

Dorigo, W. et al. 2017. “ESA CCI Soil Moisture for improved Earth system understanding: State-of-the art and future directions.” *Remote Sensing of Environment* vol. 203, pp.185–215. https://doi.org/10.1016/j.rse.2017.07.001.

Dorigo, W. et al. 2021. “The International Soil Moisture Network: serving Earth system science for over a decade.” *Hydrol. Earth Syst. Sci. Discuss.* [preprint], in review. https://doi.org/10.5194/hess-2021-2.

Dostálová, A., Doubková, M., Sabel, D., Bauer-Marschallinger, B., and Wagner, W. 2014. “Seven Years of Advanced Synthetic Aperture Radar (ASAR) Global

Monitoring (GM) of Surface Soil Moisture over Africa." *Remote Sensing*, vol. 6, pp. 7683-7707.

Edwards-Smith, A., Morrison, K., Zwieback, S., and Hajnsek, I. 2017. "Verification of the virtual bandwidth SAR (VB-SAR) scheme for centimetric resolution subsurface imaging from space." *Trans. on Geoscience and Remote Sensing*, vol. 56, no. 1, pp. 25-34.

ESA Earth Online 2022a. https://sentinels.copernicus.eu/web/sentinel/missions/sentinel-1. Accessed July 13, 2022.

ESA Earth Online 2022b. https://sentinels.copernicus.eu/web/sentinel/user-guides/sentinel-1-sar/acquisition-modes/interferometric-wide-swath. Accessed July 13, 2022.

Ferretti, A., Prati, C., and Rocca, F. 2001. "Permanent scatterers in SAR interferometry." *IEEE Trans. on Geosci. Remote Sens.*, vol. 39, pp.8–20. https://doi.org/10.1109/36.898661.

Goldstein, R. M., Zebker, H. A., and Werner, C. L. 1988. "Satellite radar interferometry: Two-dimensional phase unwrapping." *Radio Science*, vol. 23, no. 4, pp. 713-720. doi: 10.1029/RS023i004p00713.

Gruber, A., Scanlon, T., van der Schalie, R., Wagner, W., and Dorigo, W. 2019. "Evolution of the ESA CCI Soil Moisture climate data records and their underlying merging methodology." *Earth Syst. Sci. Data*, 11, pp.717–739, https://doi.org/10.5194/essd-11-717-2019.

Hahn, S., Melzer, T., and Wagner, W. 2012 "Error assessment of the initial near real-time MetOp ASCAT surface soil moisture product." *IEEE Trans. on Geoscience & Remote Sensing*, vol. 50, no 7, pp. 2556-2565.

Hallikainen, M.T., Ulaby, F. T., Dobson, M. C., and El-Rayes, M. A. 1985. "Microwave Dielectric Behavior of Wet Soil-Part 1: Empirical Models and Experimental Observations." *IEEE Transactions on Geoscience and Remote Sensing* GE-23 (1): 25–34. doi:10.1109/ TGRS.1985.289497.

Kellndorfer, J., Cartus, O., Lavalle, M. et al. 2022. "Global seasonal Sentinel-1 interferometric coherence and backscatter data set". *Sci Data* 9, 73. https://doi.org/10.1038/s41597-022-01189-6.

Lasne, Y., Paillou, P., August-Bernex, T., Ruffie. G., and Grandjean, G. 2004. "A phase signature for detecting wet subsurface structures using polarimetric L-band SAR," *IEEE Transactions on Geoscience and Remote Sensing*, vol. 42, no. 8, pp.1683-1694. doi: 10.1109/TGRS.2004.830645.

Li, Y., Zhao, K., Ren, J., Ding, Y., and Wu, L. 2014. "Analysis of the Dielectric Constant of Saline-Alkali Soils and the Effect on Radar Backscattering Coefficient: A Case Study of Soda Alkaline Saline Soils in Western Jilin Province Using RADARSAT-2 Data", The Scientific World Journal, Article ID 563015, 14 pages. https://doi.org/10.1155/2014/563015.

Lindell, D.B. and Long, D. 2016. "High-Resolution Soil Moisture Retrieval With ASCAT." *IEEE Geoscience and Remote Sensing Letters*, vol. 13, no. 7.

Liu, P.-W., Judge, J., DeRoo, R.D., England, A.W., Bongiovanni, T., and Luke, A. 2016. "Dominant backscattering mechanisms at L-band during dynamic soil moisture conditions for sandy soils." *Remote Sensing of Environment*, vol. 178, pp. 104–112.

Massari, C., Brocca, L., Ciabatta, L., Moramarco, T., Gabellani, S., Albergel, C., De Rosnay, P., Puca, S., and Wagner, W. 2015. "The Use of H-SAF Soil Moisture Products for Operational Hydrology: Flood Modelling over Italy." *Hydrology*, *2*, 2-22. https://doi.org/10.3390/hydrology2010002.

Morrison, K. 2013. "Mapping Subsurface Archaeology with SAR." *Archaeological Prospection*, vol. 20, no. 2, pp.149–160. https://doi.org/10.1002/arp.1445.

Morrison, K., Bennett, J. C., and Nolan, M. 2013. "Using DInSAR to Separate Surface and Subsurface Features." *IEEE Transactions on Geoscience and Remote Sensing*, vol. 51, no. 6, pp. 3424-3430. doi: 10.1109/TGRS.2012.2226183.

Morrison, K., and Bennett, J.C. 2013. "Tomographic Profiling – A Technique for Multi-Incidence-Angle Retrieval of the Vertical SAR Backscattering Profiles of Biogeophysical Targets." IEEE *Transactions on Geoscience and Remote Sensing*, vol. 52, no. 2, pp.1350-1355. https://doi.org/10.1080/01431161.2015.1025922.

Morrison, K., and Bennett, J.C. 2015. "Virtual Bandwidth SAR (VB-SAR) For Centimetric-Scale Sub-Surface Imaging From Space." *International Journal of Remote Sensing*, vol. 36, 1789-1808. https://doi.org/10.1080/01431161.2015.1025922.

Morrison, K., and Wagner, W. 2020. "Explaining Anomalies in SAR and Scatterometer Soil Moisture Retrievals From Dry Soils With Subsurface Scattering." *IEEE Transactions on Geoscience and Remote Sensing*, vol. 58, no. 3, pp. 2190-2197. doi: 10.1109/TGRS.2019.2954771.

Naeimi, V., Scipal, K., Bartalis, Z., Hasenauer, S., and Wagner, W. 2009. "An improved soil moisture retrieval algorithm for ERS and MetOp scatterometer observations." *Transactions on Geoscience & Remote Sensing*, vol. 47, no. 7, pp. 1999–2013.

Paillou, P., Sufyar, S., and Freeman, A. 2014. "The Chott El Djerid, Tunisia: Observation and Discussion of a SAR Phase Signature Over Evaporitic Soils," *IEEE Transactions on Geoscience and Remote Sensing*, vol. 52, no. 9, pp. 5798-5806. doi: 10.1109/TGRS.2013.2292822.

Prats-Iraola, P., Nannini, M., Yague-Martinez, N., Pinheiro, M., Kim, J.S., Costantini, M., Foumelis, M., Desnos, Y.-L., and Siniscalchi, V. 2017. "Interferometric investigations with the Sentinel-1 constellation," 2017 *IEEE International Geoscience and Remote Sensing Symposium (IGARSS)*, pp. 5537-5540. doi: 10.1109/IGARSS.2017.8128258.

Rodell, M. et al. 2004. "The Global Land Data Assimilation System," *Bulletin of the American Meteorological Society*, vol. 85, no. 3, pp. 381-394.

Thomas, N., and Nig, S. 2017 "Twentieth-Century Climate Change over Africa: Seasonal Hydroclimate Trends and Sahara Desert Expansion." *Journal of Climate Change*, vol. 31, issue 9, pp. 3349–3370. doi https://doi.org/10.1175/JCLI-D-17-0187.1.

Torres, R., Snoeij, P., Geudtner, D., Bibby, D., Davidson, M., Attema, E., Potin, P., Rommen, , B., Floury, N., Brown, M., Navas-Traver, I., Deghaye, P., Duesmann, B., Rosich,. B., Miranda, N., Bruno C., L'Abbate, M., Croci, R., Pietropaolo, A., Huchler, M., and Rostan, F. 2012. "GMES Sentinel-1 Mission", *Special Issue of Journal of Remote Sensing of Environment "The Sentinel Missions – New Opportunities for Science*", Vol. 120, pp. 9-24.

Ullmann, T., Sauerbrey, J., Hoffmeister, D., May, S.M., Baumhauer, R., and Bubenzer, O. 2019. "Assessing Spatiotemporal Variations of Sentinel-1 InSAR Coherence at Different Time Scales over the Atacama Desert (Chile) between 2015 and 2018". *Remote Sensing*, 11, 2960. https://doi.org/10.3390/rs11242960.

Wagner, W. et al. 2013. “The ASCAT soil moisture product: A review of its specifications, validation results, and emerging applications.” Meteorologische Zeitschrift, vol. 22, no. 1, pp. 5–33. https://doi.org/10.1127/0941-2948/2013/0399

Wang, Y., and Yan, X. 2017. “Climate change induced by southern hemisphere desertification”. *Physics and Chemistry of the Earth*, Parts A/B/C 102: 40–47. https://doi.org/10.1016/j.pce.2016.03.009.

Zwieback, S., Hajnsek, I., Edwards-Smith, A., and Morrison, K. 2017. "Depth-Resolved Backscatter and Differential Interferometric Radar Imaging of Soil Moisture Profiles: Observations and Models of Subsurface Volume Scattering." *IEEE Journal of Selected Topics in Applied Earth Observations and Remote Sensing*, vol. 10, no. 7, pp. 3281-3296. doi: 10.1109/JSTARS.2017.2671025.

Zwieback, S., Hensley, S., and Hajnsek, I. 2017. "Soil Moisture Estimation Using Differential Radar Interferometry: Toward Separating Soil Moisture and Displacements." *IEEE Transactions on Geoscience and Remote Sensing*, vol. 55, no. 9, pp. 5069-5083. doi: 10.1109/TGRS.2017.2702099.

Table 1. The *f* polynomial coefficients for *i*=50° and 60°. The latter is likely to be close to the Brewster angle.

Inc. Angle, *i*	***a***	***b***	***c***	***d***
50°	0.9634	-0.3363	0.0402	0.1516
60°	1.6523	-0.6039	0.0753	-0.4096

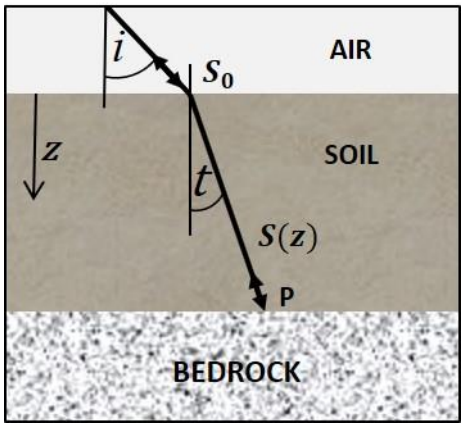

FIG. 1. Schematic of sub-surface scattering. The sub-surface layer behaves as a point scatterer at P.

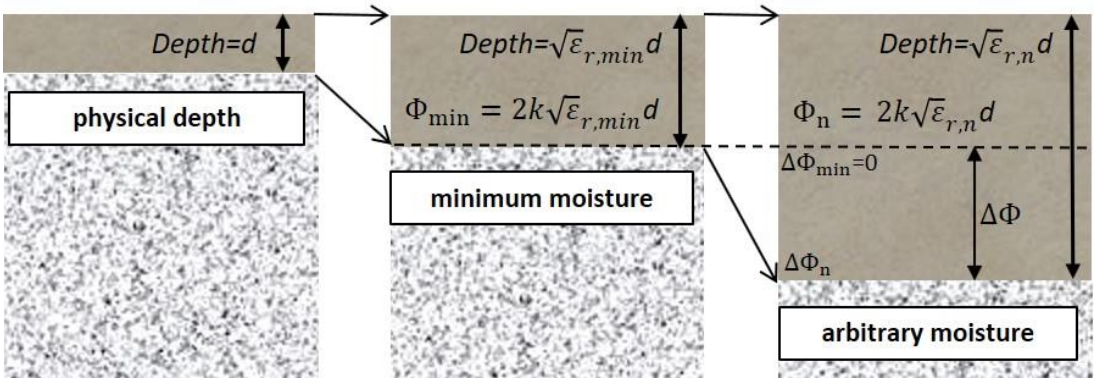

FIG. 2. Schematic of the relationship between physical depth of the soil, *d*, and its electrical depth $\sqrt{\varepsilon}_r\, d$ sensed by a radar. The upper layer represents the soil, and the lower reflecting layer is assumed to be impenetrable. The middle and right diagrams show that the apparent depth of the soil sensed by the radar increases due to moisture increase.

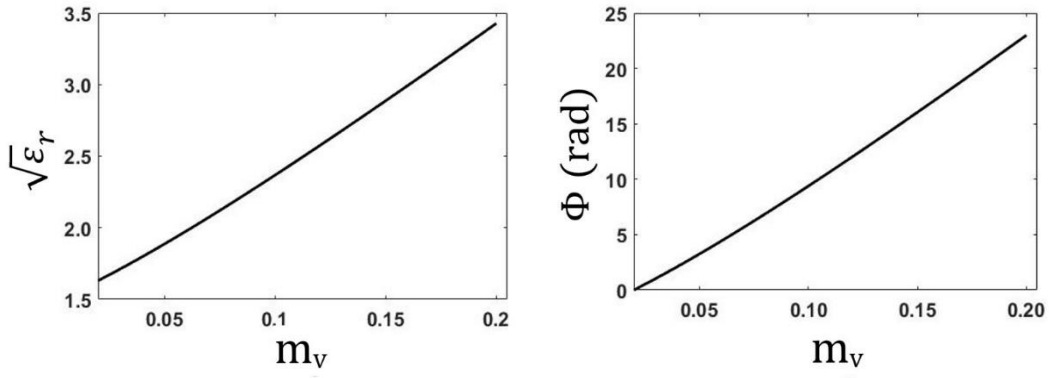

FIG. 3. The m_v - $\sqrt{\varepsilon_r}$ – Φ relationships, considering a vertically-incident 6 GHz radar wave and two-way propagation through a 0.05m thick, 100% sandy soil. Phase increase is shown relative to the minimum moisture at m_v=0.02 m^3m^{-3}.

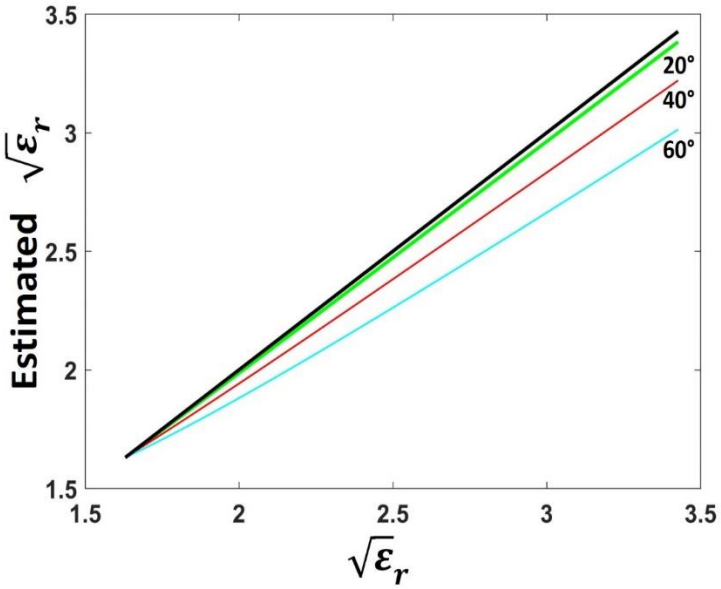

FIG. 4. The lines show how the soil dielectric term is increasingly under-estimated for increasing *i*, if the cos *t* terms in Equation 7 are ignored. The black line is for *i*=0°, and shows the correct soil dielectric term.

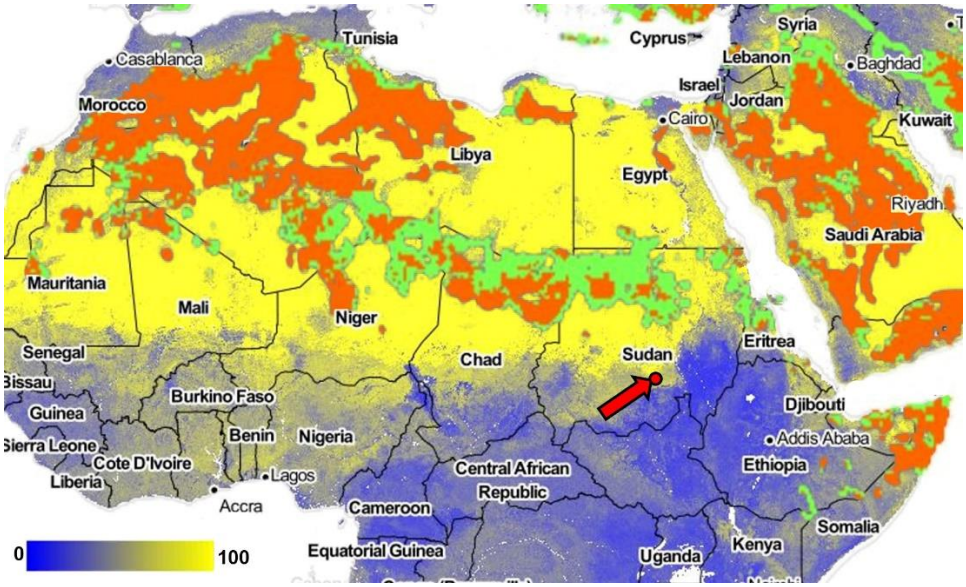

FIG. 5. Map indicating the location of areas showing persistent (brown) and temporary seasonal (green) soil moisture anomalies, and for which there are currently no reliable radar-derived soil moisture products available (modified from Morrison and Wagner 2020). It is overlain onto the CCI map of the percentage fraction of sand (yellow) and clay (blue) soil present at the surface, where the colour bar runs 0% to 100% sand (taken from 10.5281/zenodo.2525663). The location of Demokeya is indicated by the red arrow. The map encompasses 37N to 1S, and 53E to 15W

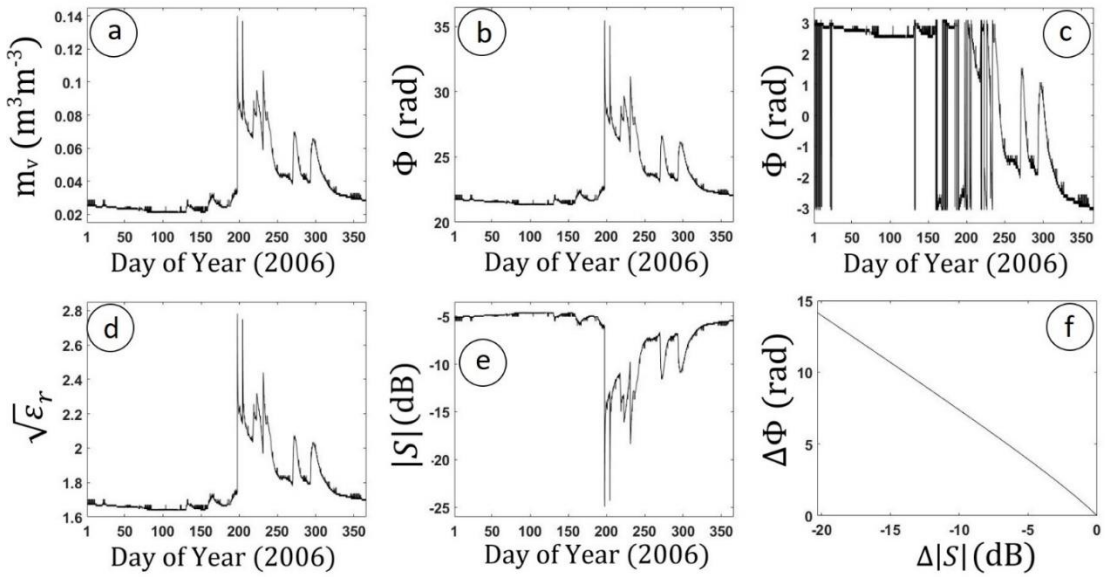

FIG.6. Model parameters for (a) m_v curve recorded at Demokeya, Sudan. The remaining panels show, for i=25°, the modelled concomitant, (b) unwrapped phase, Φ, (c) wrapped phase, Φ, (d) $\sqrt{\varepsilon_r}$, (e) 20*log$_{10}|\boldsymbol{S}|$ normalised to $20 * \log10|\boldsymbol{S_0}|$=0dB, (f) 20*log$_{10}$ $\Delta|\boldsymbol{S}|$- ΔΦ relationship, where both are differential relative to that at moisture minimum m_v=0.02 m^3m^{-3}.

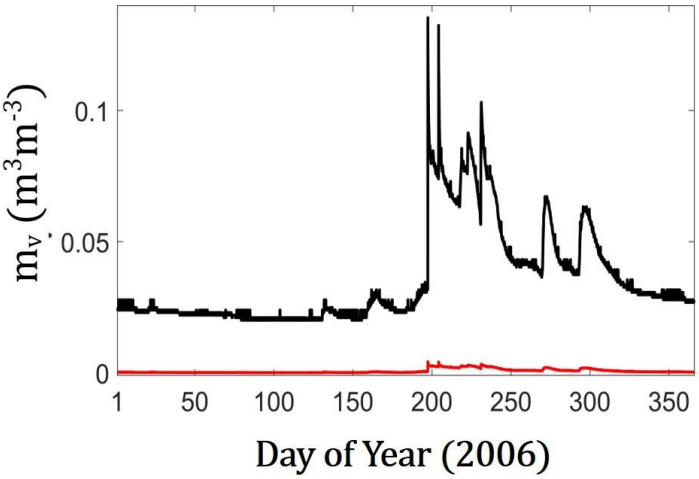

FIG. 7. The PSD-derived m_v curve is shown by the black line and the difference (measured - modelled) is shown with the lower red line. The result shown used i=25°, but the result was unchanged over the 0°-60° range investigated

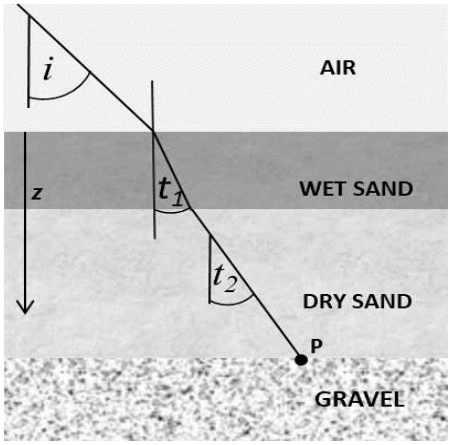

FIG. 8. The two-layer soil present in the laboratory experiment; P is presumed to be a persistent reflection point

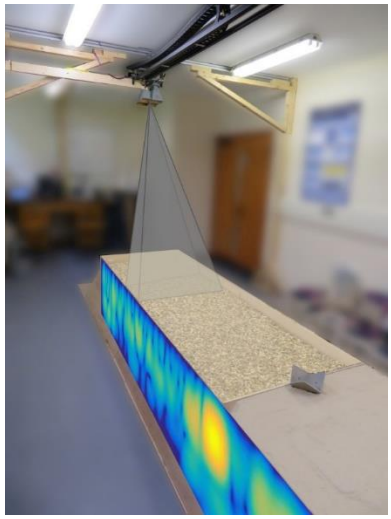

FIG. 9. Illustration of the experimental scheme. It shows the sub-surface gravel layer over the first 3m of the trough during experimental preparation. The set-up was completed by covering the gravel with a sand layer up to – and smoothing it level with – the trough edge, as has already been done for the final 1m of the trough. The trihedral acted as a reference target to correct for any system drift. The synthetic narrowing in the along-track direction by the TP scheme is highlighted, along with the revealed vertical backscatter pattern through the soil along the trough length.

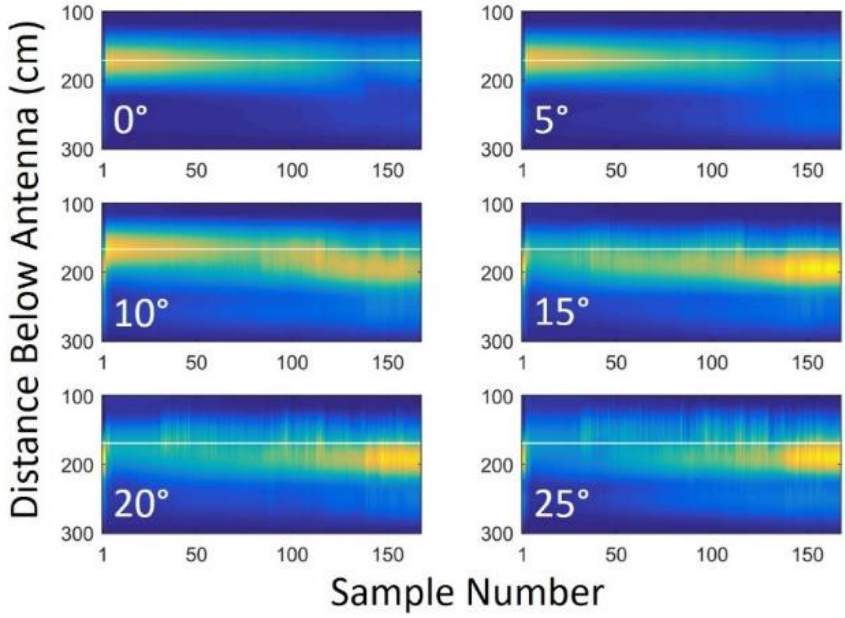

FIG. 10. Summary montage of the derived TP results with incidence angle over the course of the 15-day experiment. Each of the 167 scans contributes one column in a figure, capturing the distribution of backscatter with height. The horizontal white line indicates the position of the soil surface (reproduced from Morrison and Wagner 2020).

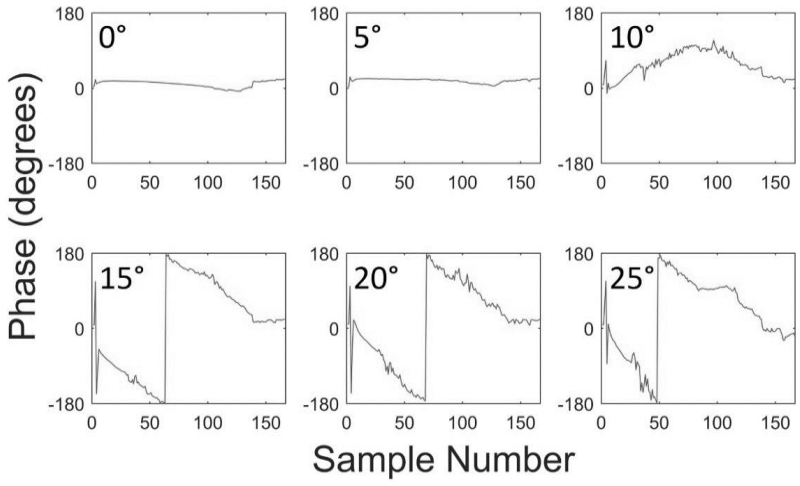

FIG. 11. Differential phase history, ΔΦ, recorded at each incidence angle

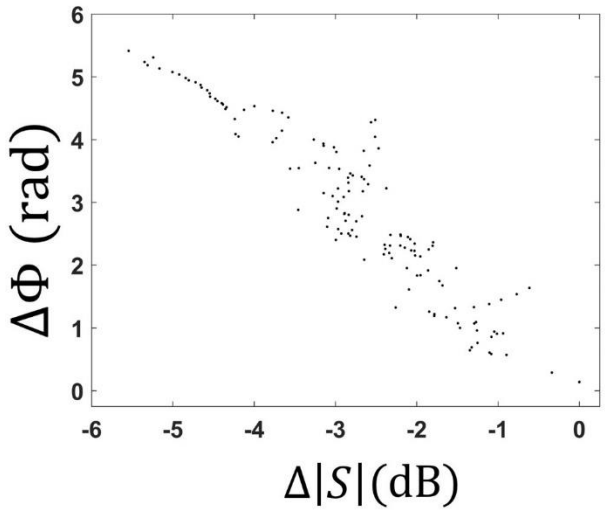

FIG. 12. The observed relationship between $\Delta|\boldsymbol{S}|$(in decibels) and $\Delta\Phi$ at i=15° for the first 140 samples of the laboratory data. $\Delta|\boldsymbol{S}|$ (dB) was set equal to 0dB at the moisture minimum.

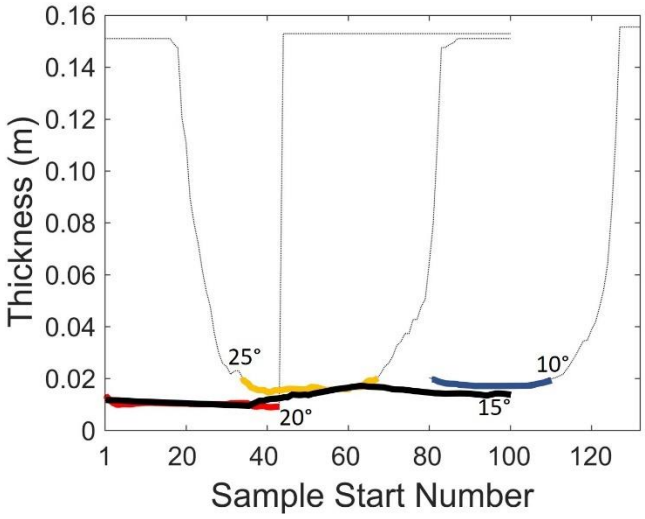

FIG. 13. Solutions for d across the laboratory timeseries. The sample start number is monotonically incremented from 1 to 101 for the 15°, 20°, 25°, cases, and 80-140 for the 10° case. Constant values around 0.15m represent no solutions found.

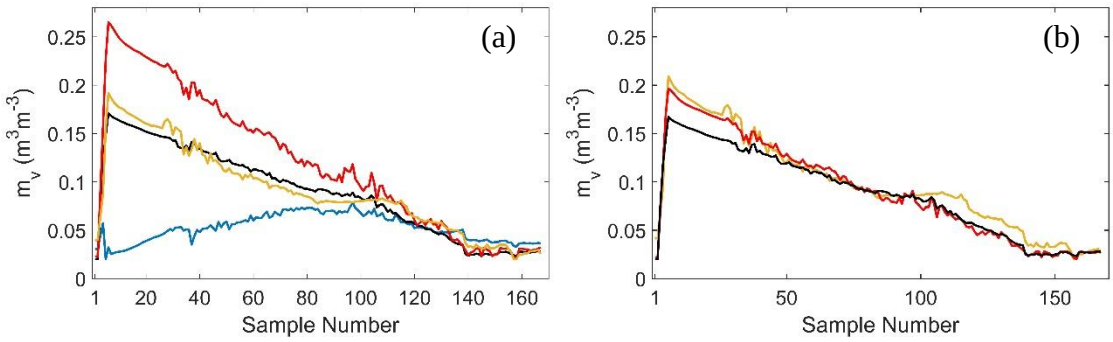

FIG. 14. (a) The retrieved m_v curves at different incidence angles; 10º (blue), 15º (black), 20º (red), 25º (yellow). The m_v estimate for the 10º case is only valid above sample 80. (b) The retrieved m_v curves using a common $\bar{d}$=0.0149m for 15º, 20º, and 25º.